Journal of the Indian Chemical Society 102 (2025) 102074

Contents lists available at ScienceDirect

Journal of the Indian Chemical Society

journal homepage: www.journals.elsevier.com/journal-of-the-indian-chemical-society

High-performance flexible supercapacitors based on porous carbon derived from Setaria viridis stalks

Wei Jin [a,1], Wen Li [a,1], Rongke Sun [a], Xiao Zhang [a], Mingyu Wu [a,d], Hafiza Sana Haider [a], Dongliang Ma [d], Yanqing Ma [a,b,c,e,*], Lei Ma [a,b,e,**]

[a] *Tianjin International Center for Nanoparticles and Nanosystems, Tianjin University, Tianjin, 300072, PR China*
[b] *Tianjin Key Laboratory for Low-dimensional Electronic Materials and Advanced Instrumentation, Tianjin, 300072, PR China*
[c] *School of Precision Instrument and Opto-electronics Engineering, Tianjin University, Tianjin, 300072, PR China*
[d] *School of Physical Science and Technology, Xinjiang University, Urumqi, 830046, PR China*
[e] *Haihe Laboratory for Low-dimensional Electronic Materials, Add 1 to No.57 Wujiayao Street, Hexi District, Tianjin, 300074, PR China*

ARTICLE INFO

Keywords:
Setaria viridis stalk
Activated carbon
Flexible
Supercapacitor

ABSTRACT

The renewable biomass waste as an activated carbon source for flexible supercapacitors is a current research hotspot. Herein, the Setaria viridis stalk-based activated carbon (SVS) materials were synthesized by carbonization and KOH activation at different temperatures (800°C, 900°C and 1000°C). The assembled SVS-based electrode can deliver a high specific capacitance of 248 F g^{-1} at 2 mV s^{-1} in 1 M H_2SO_4 aqueous electrolyte. When flexible supercapacitors were assembled with PVA/H_2SO_4 polymer gel, the device demonstrated a maximum capacitance of 690 F g^{-1} (at 2 mV s^{-1}), excellent cycle stability (89 % capacitance retention even after 10,000 cycles) and energy density (8.28 W h kg^{-1}). Most importantly, the as-fabricated device retained its electrochemical performance well, even under harsh conditions such as bending, rolling and twisting.

1. Introduction

Flexible and high-performance energy storage devices are urgently needed to meet the growing demands of wearable electronics, smart sensors, and portable systems. Among various candidates, supercapacitors have garnered significant attention due to their fast charge–discharge rates, high power densities, and long cycle life [1–8]. However, achieving a simultaneous combination of high energy density, mechanical flexibility, and environmental sustainability are key and urgent problems for practical application in electrochemical energy storage devices [9]. Conventional electrode materials and organic electrolytes commonly used in supercapacitors are often costly, toxic, and incompatible with flexible device configurations [10].

To address these issues, biomass-derived porous carbon materials have emerged as promising electrode materials due to their inherent sustainability, adjustable pore structure, very good chemical and thermal stability and low cost [11–19]. A variety of biomass precursors, including coconut shells [20], straw [21], metaplexis shell [22] and agricultural waste, have been successfully converted into activated carbon with tailored pore architectures and excellent electrochemical performance. Nonetheless, many of these biomass sources either lack mechanical resilience or involve complex processing. Therefore, achieving excellent bending stability and high capacitance in all-solid supercapacitors remains challenging, leaving ample room for further development in flexible applications.

In this context, Setaria viridis, a ubiquitous fast-growing weed with minimal agricultural value, offers a unique opportunity. Its stalks are composed of naturally aligned vascular bundles with a hollow tubular morphology, providing a favorable template for constructing interconnected porous carbon frameworks. Utilizing such underexploited agricultural residues not only reduces production costs and environmental burden but also enables the design of 3D carbon skeletons with enhanced ion transport channels and mechanical integrity.

In this study, we report the synthesis of porous carbon from Setaria viridis stalks via direct carbonization and KOH activation. The resulting materials exhibit tunable pore structures and favorable graphitic features depending on the activation temperature. When applied in flexible supercapacitors using a PVA/H_2SO_4 gel electrolyte, the best-performing

---

* Corresponding author. Tianjin International Center for Nanoparticles and Nanosystems, Tianjin University, Tianjin, 300072, PR China.
** Corresponding author. Tianjin International Center for Nanoparticles and Nanosystems, Tianjin University, Tianjin, 300072, PR China.
E-mail addresses: mayanqing@tju.edu.cn (Y. Ma), lei.ma@tju.edu.cn (L. Ma).

[1] Those authors contributed equally to this paper.

https://doi.org/10.1016/j.jics.2025.102074
Received 28 April 2025; Received in revised form 2 August 2025; Accepted 27 August 2025
Available online 28 August 2025

material (SVS-900) delivers a high specific capacitance of 690 F g^{-1}, exceptional cycle stability (89 % retention over 10,000 cycles), and robust mechanical tolerance under bending and twisting. This work not only introduces a cost-effective and sustainable biomass precursor but also demonstrates a scalable strategy to develop high-performance flexible energy storage devices suitable for next-generation electronics.

2. Experiment

2.1. Synthesis

The Setaria viridis stalks utilized in this study were harvested from the Tianjin University campus. The chemicals utilized in this study were of analytical reagent grade and were used without any additional purification steps.

The process is listed in Fig. 1. The Setaria viridis stalks were rinsed thoroughly with distilled water and dried at 60 °C for 12 h. Subsequently, the dried stalks were finely chopped, rinsed again with distilled water, and dried at 80 °C for another 12 h. The prepared raw materials were then subjected to carbonization in a tubular furnace under argon atmosphere for a duration of 1 h at 400 °C, resulting in the sample designated as SVS-400. Next, the SVS-400 sample was combined with KOH in a mass ratio of 1:4 for the process of activation. Starting from room temperature, the temperature was increased at a rate of 5 °C min^{-1} to activation temperatures of 800 °C, 900 °C, and 1000 °C, respectively, and held for 1 h. Finally, the activated materials were rinsed with deionized water to neutral and named as SVS-800, SVS-900 and SVS-1000 respectively. In addition, The Setaria viridis stalk-based porous carbon materials SVS-3-900 and SVS-5-900 were prepared under the same conditions at an activation temperature of 900 °C using different ratios of M_C:M_{KOH} = 1:3 and 1:5, respectively, in order to compare the effect of activation ratios on structural properties.

2.2. Preparation of electrodes and all-solid-state supercapacitor

Activated carbon material, acetylene black and PTFE binder were mixed in the ratio of 8:1:1 by mass and then an appropriate amount of anhydrous ethanol was added with constant stirring to homogenize the mixture in a mortar and pestle. The paste obtained was pressed into a uniform thin sheet electrode with a diameter of 0.8 cm and 300 μm thickness using a tablet press, and then dried with oven at 110 °C for a duration of 4 h. The mass of each electrode was controlled to be around 2 mg. The symmetric supercapacitor is assembled from a CR2032 cell case by placing two electrodes of the same mass on the surface of hydrophilic carbon paper, with a polypropylene film (polypropylene film, thickness: 25 μm, poriness: 41–55 %) acting as a diaphragm. Then, a conventional symmetrical supercapacitor was assembled and encapsulated under 10 MPa pressure in the order of stainless steel case, spacer, electrode set, spacer, and case, and the measurements were repeated at least three times for each set.

The all-solid-state flexible supercapacitor was assembled with two identical electrodes prepared according to the above-mentioned method. The electrolyte is PVA/H_2SO_4 gel. To prepare the PVA/H_2SO_4 gel, 1 g PVA was mixed with 7 mL deionized water and stirred at 80 °C until the mixture became clear. After that, 3 mL H_2SO_4 solution (3.4 M) was slowly added to the above mixture. Then a transparent gel is obtained as an electrolyte after stirring at 60 °C for 0.5 h. Two electrodes were soaked in the PVA/H_2SO_4 gel at 60 °C for 4 h, and then positioned head-to-head. Finally, the all-solid-state supercapacitor was fabricated successfully after packaging.

2.3. Characterization

The samples were examined for their morphology and microstructure using a Scanning Electron Microscope (SEM, SU3500, Japan). Raman spectra were collected using a Confocal Raman spectrometer system with an excitation wavelength of 532 nm. X-ray diffraction patterns (XRD) were recorded using a Bruker D8 advance X-ray diffractometer equipped with a Cu-Kα radiation source ($\lambda = 1.57418$ Å). The scanning angle range was set from 5 to 90°, with a scanning rate of 0.04° s^{-1}, and the instrument operated at 25 mA and 35 kV.

2.4. Electrochemical measurements

Cyclic voltammetry (CV), electrochemical impedance spectroscopy (EIS) and charge-discharge performance (CP) were carried out on a CHI 760 E electrochemical workstation. The voltage range for CV testing is from 0 V to 0.8 V. The frequency range for EIS testing is from 0.01 to 100 kHz with 5 mV amplitude for AC voltage.

According to the CV curves, the specific capacitance of supercapacitor can be calculated from the following equation:

$$C_E = \frac{1}{2} \times \frac{\int I(V) \times dV}{\Delta V \times v} \tag{1}$$

where C_E (F·g^{-1}) is the device specific capacitance, I (A·g^{-1}) is the current density, V (V) is the applied voltage, $\int I(V)dV$ is the mathematical integral area of CV curve, ΔV (V) and ν (mV·s^{-1}) refer to the operating voltage window and scan rate respectively.

According to the GCD curves, the electrode specific capacitance (C_S, F g^{-1}), the device specific capacitance (C_D, F g^{-1}), Energy density (E, Wh kg^{-1}) and Power density (P, W kg^{-1}) can be calculated based on the following equations from the charge-discharge cures:

$$C_S = 4 \times \frac{I_d \times \Delta t}{\Delta V \times m} \tag{2}$$

$$C_D = \frac{I_d \times \Delta t}{\Delta V \times m} \tag{3}$$

$$E = \frac{1}{2} C_D \times \Delta V^2 \times \frac{1}{3.6} \tag{4}$$

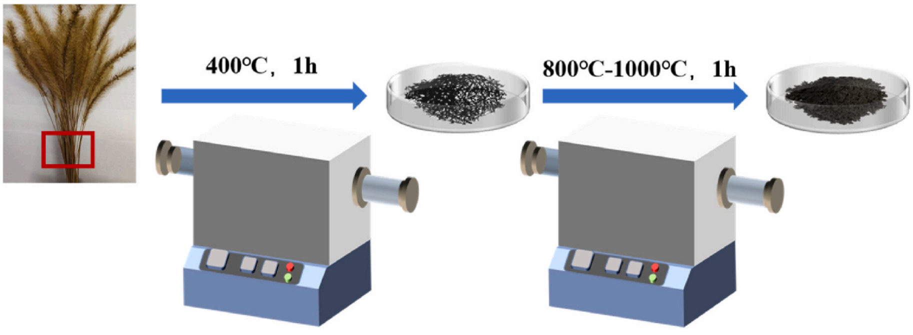

Fig. 1. The chart of porous carbon material preparation.

$$P = \frac{E}{\Delta t} \times 3600 \tag{5}$$

Where ΔV (V) is the discharge voltage range, m (g) represents the mass of active carbon materials for both electrodes, I_d (A) indicates the discharge current, Δt (s) signifies the discharge time. The specific capacitance described in this paper is the electrode specific capacitance.

3. Results and discussion

Fig. 2(A–C) shows the SEM images of raw materials of setaria viridis stalks. It can be seen that the stalks show a hollow tubular structure with the wall thickness of 200–350 μm. This hollow tubular wall has a typical vascular bundle structure, the wall thickness of which is ~1–2 μm. As shown in Fig. 2(D–E), after carbonization at 400 °C, the typical long vascular bundle structure of the raw material is retained, and the porous structure is exposed with obvious large pores uniformly arranged on the tube wall in Fig. 2F. In addition, the walls of vascular bundles are thinner, about 500 nm. SVS-400 not only inherits the vascular bundle structure of the original materials but also derives a large number of holes on the walls of the vascular bundles, making it an open interconnected hollow carbon skeleton. This connected hollow through tubular structure facilitates the activator to fully penetrate into the material during the activation process, effectively improves the activation rate, and is conducive to the formation of carbon materials with abundant multilevel pore structure and high electrical conductivity.

After high-temperature etching, the sample as a whole has a porous honeycomb structure. Comparison of Fig. 3(C,F,I) with the increase in temperature, the activation effect is enhanced, the pore size increases significantly (Fig. 3E), the surface shows a uniformly arranged and orderly porous honeycomb pore structure, which provides a channel for the ion transport, and the temperature is increased to 1000 °C in the middle at this time the material is severely corroded by KOH, the pore structure collapses, and there are also some carbon flakes blocked in the pore, which makes it more difficult for ions to enter the pore, which is not conducive to the ion transport of ions. From Fig. 3(D–F) and Fig. S1, it can be clearly seen that there is a sharp contrast between the amount of activator, SVS-900 is more continuous and abundant, and M_C:M_{KOH} = 1:4 is the optimal amount of KOH. As shown in Fig. S2A, the isotherm of SVS-900 exhibits a typical Type I profile, indicating a predominantly microporous structure, with a specific surface area of 1555.36 $m^2\ g^{-1}$. Furthermore, the pore size distribution curve (Fig. S2B) reveals that the pores are primarily concentrated below 1 nm, which facilitates effective surface area utilization and promotes charge accumulation [23]. Moreover, Table S1 provides quantitative EDS analysis results for carbon and oxygen elements in SVS-800,900,1000.

Fig. 4A and Fig. S3 shows the XRD patterns of the prepared activated porous carbon materials. The peak at ~20–26° is correlated to (002) crystal plane of amorphous carbon and the weak peak at ~43° is correlated to (100) crystal plane of graphite [24,25]. The weak peaks indicate that all samples have low crystallinity and amorphous structure, which is favorable for ion storage to enhance the electrochemical performance [26,27]. It can be seen that the diffraction intensity and diffraction angle of (002) peak increases with the increasing activation temperature. The displacement of (002) peak increase is concerned with the structural change of the porous carbon materials [24]. When the activation temperature increases, the diffraction peak of (002) crystal plane moves to a higher diffraction angle, indicating that the lattice is compressed. According to the Bragg equation, the distances between (002) crystal planes at SVS-900 and SVS-1000 materials are calculated as 0.368 nm and 0.354 nm. This corresponds with the graphite crystal of 0.335 nm. The rise in diffraction intensity at lower scattering angles suggests a greater presence of micropores in the samples [28,29]. Similarly, the absence of additional peaks indicates the successful conversion of biomass waste into carbon materials and high purity of the samples prepared in this manner.

Fig. 4B shows the Raman spectra of three activated porous carbon materials. All three samples exhibit prominent peaks at 1341 cm^{-1} and 1574 cm^{-1}, corresponding to the D band and G band, respectively. The D peak is associated with the degree of disorder or structural defects, while the G peak is related to the ordered arrangement of carbon atoms. The intensity ratio of the D band and the G band (I_D/I_G) reflects the degree of disorder in atom alignment, which implies that the lower the value of I_D/I_G, the higher the degree of graphitization. The I_D/I_G values for the three samples, SVS-800, SVS-900, and SVS-1000, are 0.98, 0.99, and 0.39 respectively. The values of I_D/I_G increase and then decrease with the increase of temperature, which indicates that the SVS-900 sample have more carbon layer defects that provide more active centers and can realize more excellent capacitive performance [30,31]. This indicates that the sample SVS-1000 exhibits the highest degree of graphitization. Additionally, SVS-1000 also exhibits a prominent 2D band at 2675 cm^{-1}, which indicates the presence of 3D graphene and few-layer graphene [32]. The Raman spectra of SVS-3-900 and SVS-5-900 are shown in Fig. S4, and their I_D/I_G was calculated to be 1.17 and 1.09, respectively, which obviously have a lower degree of graphitization.

The electrochemical properties of SVS-800,900,1000 were systematically tested since the above characterization of the morphology and structure is more desirable when the mass ratio of carbon material and KOH is 1:4. Fig. 5 is the electrochemical performance curves of supercapacitors with electrodes made of three different porous carbon materials, tested using a dual-electrode system with a potential window of

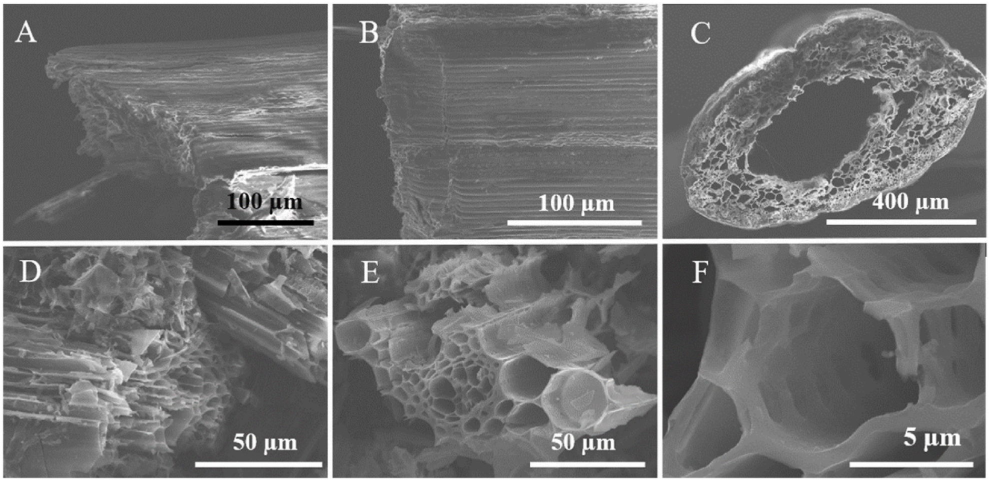

Fig. 2. The SEM images of (A–C) the raw materials and (D–F) the carbonized products at 400 °C of setaria viridis stalks at various magnifications.

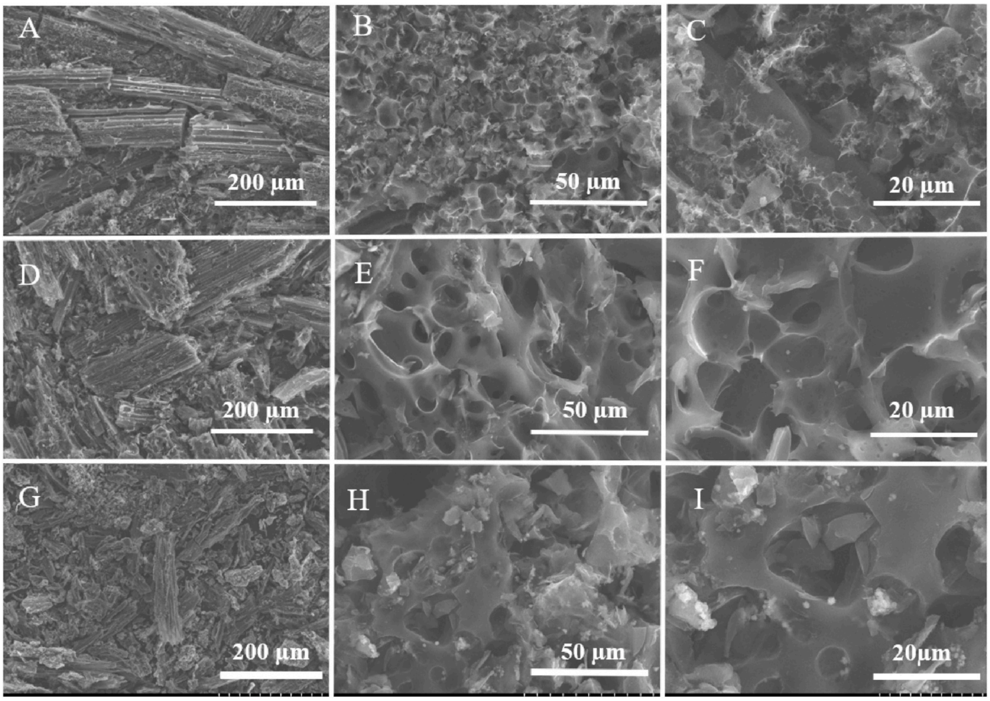

Fig. 3. The SEM images of porous carbon materials at various activation temperatures. (A–C) SVS-800, (D–F) SVS-900, (G–I) SVS-1000.

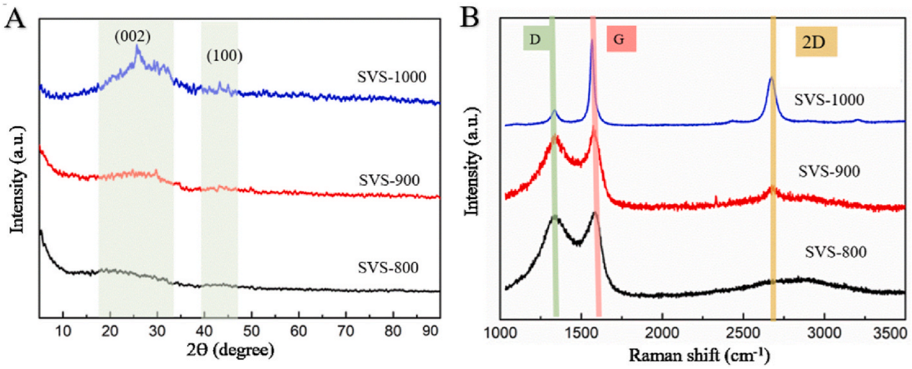

Fig. 4. (A) XRD patterns and (B) Raman spectra of SVS-800, SVS-900 and SVS-1000.

0.8 V in a 1 M H_2SO_4 aqueous electrolyte. The capacitance value is directly proportional to the area enclosed by the CV curve, and the nearly rectangular shape of the CV curve indicates better capacitance characteristics and lower internal resistance. Fig. 5(A,C,E) are the CV curves of SVS-800, SVS-900 and SVS-1000 at various scan rates ranging from 2 to 100 mV s^{-1}. It is evident that the CV curves maintain a nearly rectangular shape even when the scan rate is 100 mV s^{-1}, indicating rapid mass diffusion. The specific capacitances of SVS-800, SVS-900 and SVS-1000 are 232 F g^{-1}, 248 F g^{-1} and 126 F g^{-1} at 2 mV s^{-1}, respectively.

Fig. 5B, D, F are the charge and discharge curves of SVS-800, SVS-900 and SVS-1000 measured at various current densities, respectively. The curves are isosceles triangles at 0–0.7 V, and there is no significant voltage drop, which indicates a good double layer capacitance. A longer discharge time typically indicates a higher specific capacitance of the material [33,34]. At the same current density, SVS-900 presents a highly symmetric curve with the longest discharge time, which shows the best capacitive performance. As the current density increases, the charging time decreases and the shape of the curve remains constant. At 0.2 A g^{-1}, the specific capacitances of SVS-800, SVS-900 and SVS-1000 are 212 F g^{-1}, 230 F g^{-1} and 156 F g^{-1} respectively (Fig. 5(B,D,F)). Compared to commercial activated carbon (153 F g^{-1} at 1 A g^{-1}) [35], SVS-900 (208 F g^{-1} at 1 A g^{-1}) has a much higher capacitance and shows great utilization in commercial applications.

In addition to porosity and surface chemistry, electrical conductivity is one of the factors that have a strong influence on capacitive behavior [36,37]. Fig. 6 (A) shows the Nyquist curves of different symmetric supercapacitors, and the equivalent series resistances of SVS-800, SVS-900 and SVS-1000 are 1.06 Ω, 1.36 Ω and 1.55 Ω, respectively, fitted according to the equivalent circuit diagrams, which indicates that these electrodes have good conductivity. In addition, the charge transfer resistance of SVS-900 (0.22 Ω) is smaller than that of SVS-800 (0.96 Ω) and SVS-1000 (3.71 Ω). From the above phenomena, it can be seen that the Setaria viridis stalks-based porous carbon prepared at 800 °C has richer mesopores, which can provide fast ion-transfer channels and thus exhibit lower resistance and better performance. And the lines in the low-frequency region of SVS-900 are steeper and more vertical, which indicates that has the ability of ion diffusion and migration efficiently and exhibits better capacitive performance. As calculated from Eq. (6) [38]:

$$\tau = C_D R_{ct} \tag{6}$$

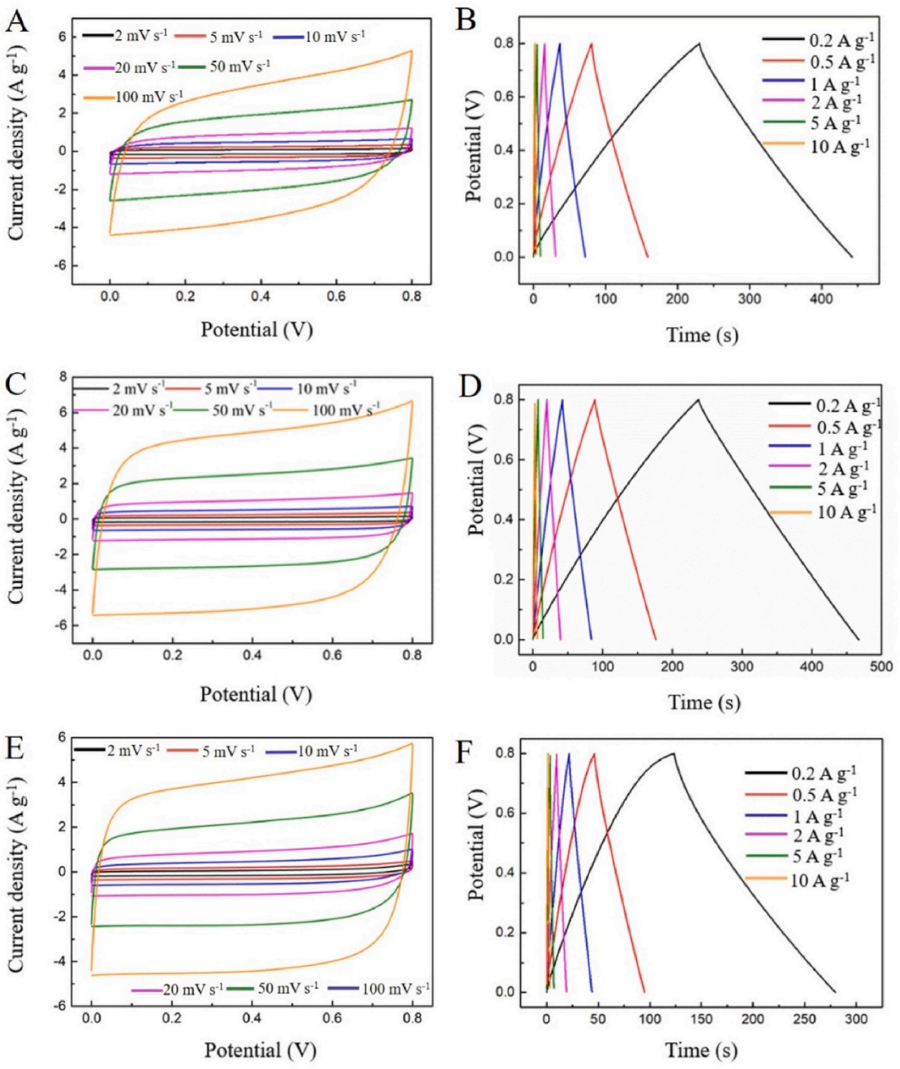

Fig. 5. (A, C, E) CV curves of SVS-800, SVS-900 and SVS-1000 at various scan rates, (B, D, F) CP curves of SVS-800, SVS-900 and SVS-1000 at various current densities (H_2SO_4 aqueous electrolyte).

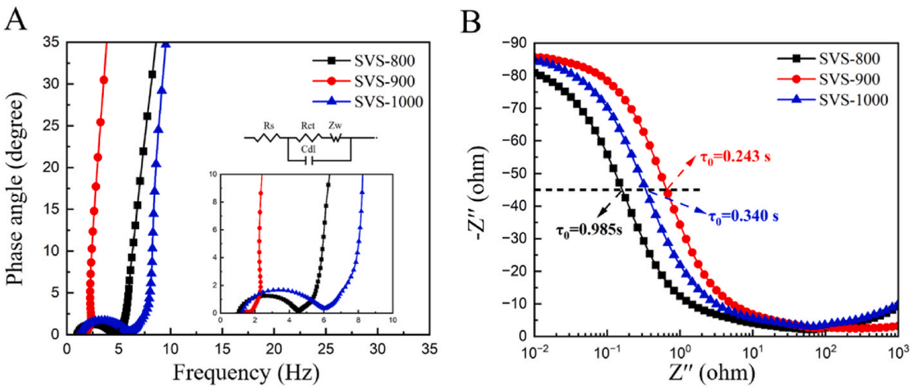

Fig. 6. For the SVS-800, SVS-900, and SVS-1000: (A) Nyquist plots (inset: Nyquist plots in the high frequency region), (B) bode plots of phase angle vs. frequency.

The time constants of SVS-800, SVS-900 and SVS-1000 symmetric supercapacitor devices are 0.30 s, 0.28 s and 0.31 s, respectively. The smallest time constant of SVS-900 indicates that its device has better response capability.

A key parameter in Fig. 6B is the relaxation time constant τ_0. Calculating τ_0 based on f_0 at a phase angle of −45°, the SVS-900 has a smaller τ_0 value than the SVS-800 and SVS-1000, which is much lower than that of a conventional activated carbon electrochemical capacitor [39]. The lower τ_0 implies a faster transport rate of electrolyte ions and better capacitive performance at high current densities [40].

In addition, the electrochemical kinetics of SVS-900//SVS-900 symmetric supercapacitors were investigated based on the CV curves using power-law equations [41]:

$$i = kv^b \tag{7}$$

Where i is current, v is scan rate, and k and b are adjustable parameters. Typically, diffusion-controlled processes are exhibited when $b = 0.5$ and surface-controlled processes are exhibited when $b = 1$ [42]. Fig. 7A shows that the device exhibits a b value of 0.89, indicating that it is influenced by a combination of surface-controlled and diffusion-controlled processes, with a b value close to 1 indicating that the surface-controlled processes dominate. In order to understand the contribution of diffusion and surface adsorption to the overall performance, further calculated the surface-controlled capacitance ratio and diffusion-controlled capacitance ratio of the SVS-900//SVS-900 symmetric supercapacitor based on the CV curves of the SVS-900//SVS-900 symmetric supercapacitor by using equation (7) [43,44].

$$i(V) = k_1 v + k_2 v^{1/2} \tag{8}$$

In this equation, $k_1 v$ and $k_2 v^{1/2}$ are the capacitive and diffusive contributions, respectively. The results show that the surface control ratio gradually increases from 68 % to 94 % with increasing scan rate as shown in Fig. 7C, which may be attributed to the fact that the diffusion process is hindered and the surface control process dominates at high scan rates, which favors a more superior cycling stability.

Then the porous carbon materials obtained from setaria viridis straws were assembled into flexible supercapacitors with solid state electrolyte PVA/H_2SO_4. Fig. 8(A–C) shows the CV curves of SVS-800, SVS-900 and SVS-1000 respectively. It can be observed that all CV curves closely resemble nearly symmetric rectangles, indicating ideal capacitance behavior based on ion adsorption and exchange. More importantly, the CV curves of the flexible supercapacitors reveal a symmetrical semi-rectangular shape even at a high scan rate of 100 mV s^{-1}. This demonstrates the low intrinsic resistance of the working electrodes in the cell device. At 5 mV s^{-1}, the specific capacitances of SVS-800, SVS-900 and SVS-1000 are 366 F g^{-1}, 518 F g^{-1} and 263 F g^{-1} and the specific capacitance of SVS-900 can reach 690 F g^{-1} at 2 mV s^{-1}. As shown in Fig. 8D, the SVS-900 reveals significantly higher specific capacitance at the same scan rate than it in the SVS-800 and SVS-1000 samples.

Besides, as shown in Fig. 9(A–C), GCD curves under different current densities are studied. The GCD curves of all samples show approximate isosceles triangle shapes at 0–0.7 V, indicating the good electrochemical reversibility of the supercapacitor [45,46]. The discharge time of SVS-900 is also significantly longer than the other two samples, indicating that SVS-900 has the maximum specific capacitance at the same current density, with a specific capacitance of 487 F g^{-1} and 234 F g^{-1} at current densities of 2 A g^{-1} and 10 A g^{-1}. Consistent with the CV test results, SVS-900 has superior capacitance performance, the superior capacitive performance of SVS-900 was analyzed because of the interconnected porous structure that provides easy transportation channels for electrolyte ions, which facilitates rapid electron transfer and charge accumulation on the electrode surface. The GCD curve of SVS-900 shows no significant decrease in internal resistance (IR) observed at high current densities. This indicates characteristics such as low equivalent series resistance, excellent rate performance, and strong capability for rapid charge propagation.

Electrochemical impedance spectrometry (EIS) was used to investigate the electron/ion transport process of all-solid-state supercapacitors. The factors affecting the resistance ESR in the device mainly come from the resistance of the electrode material, the interface resistance between the electrode material and the collector, the ion diffusion impedance when ions enter the pores, the ion migration resistance when ions pass through the diaphragm, and the ion migration impedance in the electrolyte. High internal resistance will limit the power capacity of the capacitor [47–49]. Fig. 9D is the EIS of SVS-800, SVS-900 and SVS-1000 at 0.01 Hz–100 kHz. In the high-frequency region, the intercept between the real part of the Z-axis and the semicircle represents the impedance value. The diameter of the semicircle represents the sum of the three parts (the resistance of the electrolyte, the resistance of the carbon material and the resistance between the electrode and the collector) [50]. The larger the semicircle, the higher the electron transfer

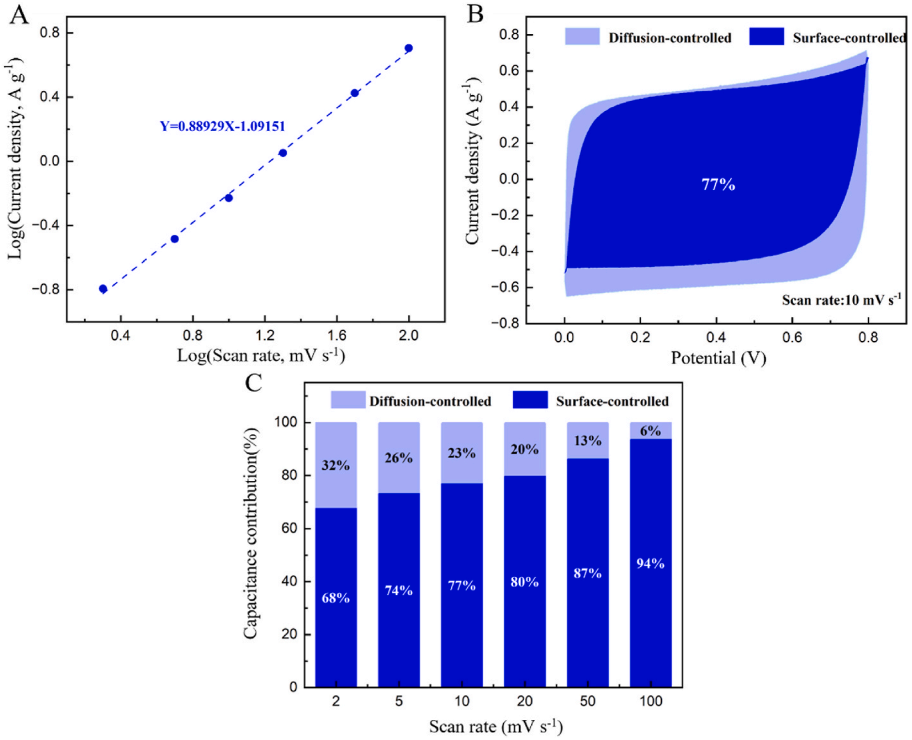

Fig. 7. SVS-900//SVS-900 symmetric supercapacitors: (A) b value calculated by power law equations, (B) energy storage contribution by surface-controlled and diffusion-controlled processes at 10 mV s^{-1}, (C) capacitance contribution ratio at different scan rates.

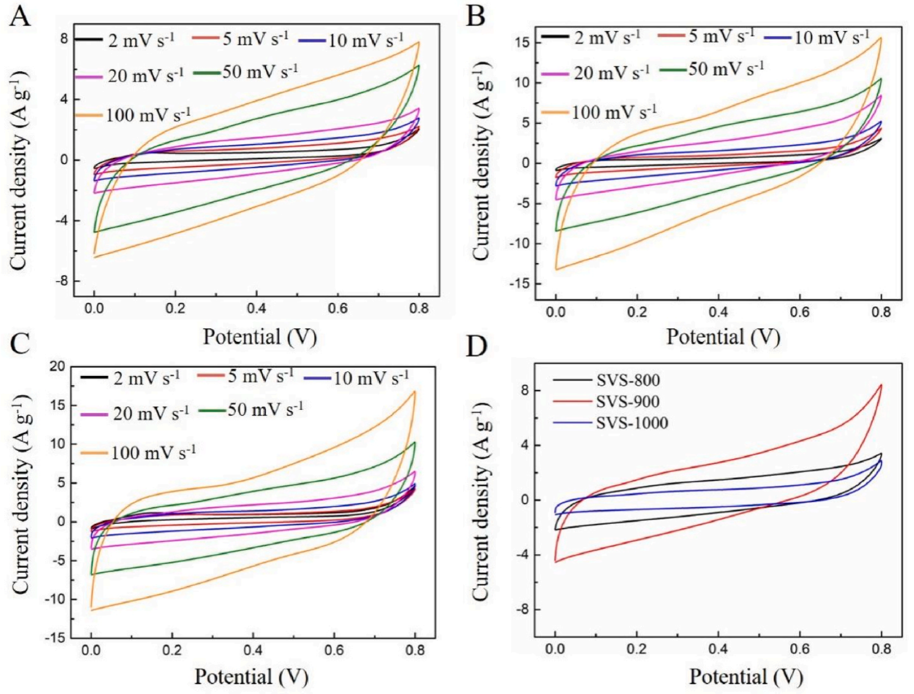

Fig. 8. (A–C) CV curves of SVS-800, SVS-900 and SVS-1000, (D) CV curves of SVS-800, SVS-900 and SVS-1000 at 20 mV s^{-1} (PVA/H_2SO_4).

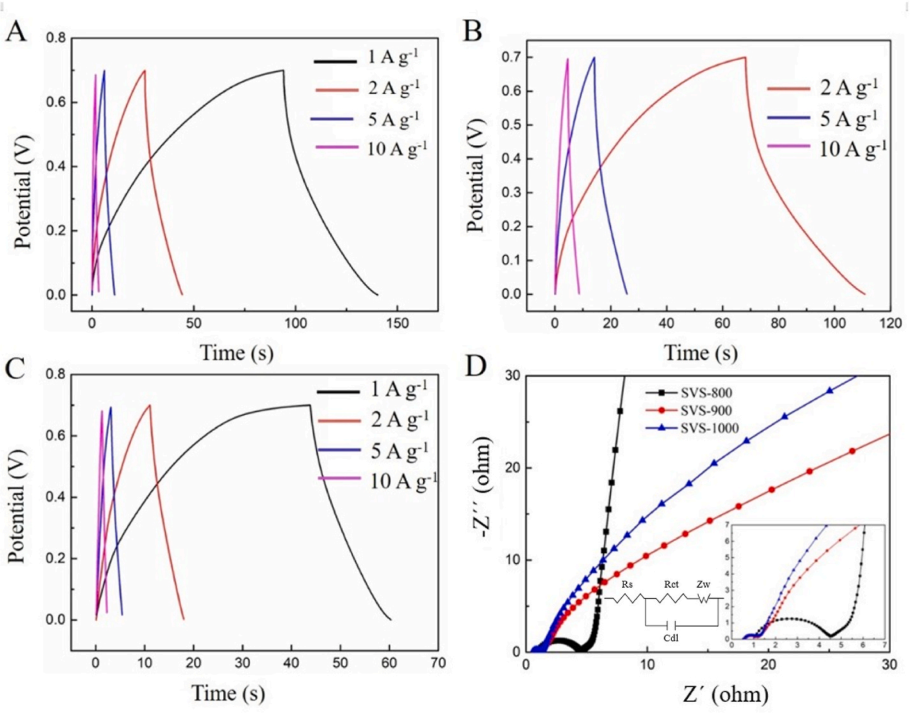

Fig. 9. (A–C) CP curves and (D) EIS curves of SVS-800, SVS-900 and SVS-1000 (PVA/H_2SO_4).

resistance and the worse the conductivity [51–53]. The R_s of SVS-800, SVS-900 and SVS-1000 are 1.25 Ω, 0.65 Ω and 0.59 Ω. The R_{ct} is 2.9 Ω, 0.36 Ω and 0.54 Ω. The lower internal resistance of the SVS-900 device results in more rapid transport and transfer of ions across the electrode surface, suggesting that the lower resistance makes an important contribution to the electrochemical performance of the capacitor [54]. And we can see that the total resistance of SVS-900 is the smallest among three materials, which results in higher specific capacitance.

Energy density and power density are the two primary criteria used to evaluate the performance of a supercapacitor. Fig. 10A presents the Ragone plot of the SVS-900-based flexible supercapacitor, clearly illustrating the energy–power trade-off. The device delivers a maximum energy density of 8.28 W h kg^{-1} at a power density of 3500 W kg^{-1}, which is competitive with or superior to most previously reported biomass-derived flexible devices. These results reflect the favorable ion

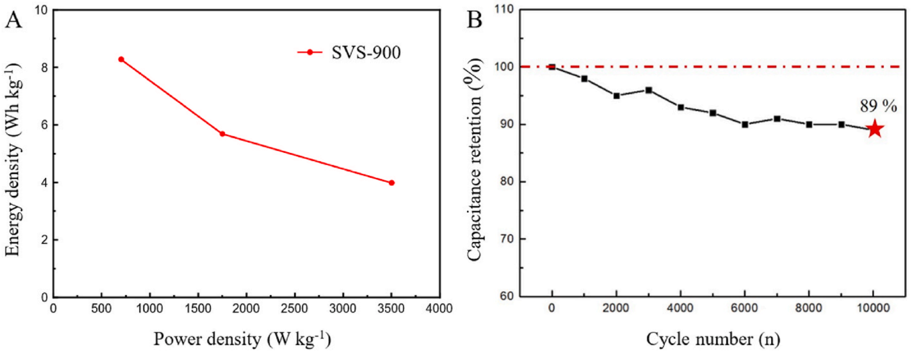

Fig. 10. (A) Ragone plot of the SVS-900 supercapacitor at various current densities, (B) Cycle stability at a current density of 10 A g^{-1} after 10,000 cycles.

transport kinetics and charge storage capability of the SVS-900 architecture. Fig. 10B depicts the variation in specific capacitance of the SVS-900 supercapacitor with increasing charge-discharge cycles at a current density of 10 A g^{-1}. The initial coulombic efficiency of 91 % (10 A g^{-1}) combined with 89 % capacity retention after 10,000 cycles demonstrates excellent long-term cycle stability [55–58]. To further assess the performance of the SVS-900-based device, we compared it with other reported biomass-derived carbon-based supercapacitors. As summarized in Table S2, our material exhibits higher specific capacitance and competitive cycling stability under a two-electrode solid-state configuration.

To be better applied in wearable electronic devices, the mechanical strength of flexible supercapacitors must be verified under harsh conditions. Fig. 11A shows the CV curves at various bending angles (0°, 45°, 90°, and 135°) at a scan rate of 20 mV s^{-1}. From the figure, it can be observed that the CV curves at various bending angles exhibit a high degree of overlap, and their shapes closely resemble rectangles without significant deformation, which shows ideal capacitive behavior. Compared with the flat state before bending, the specific capacitance is 112 %, 104 % and 87 % of the flat state respectively. The increase in specific capacitance may be attributed to some extent of damage to the SVS-900 skeleton during the bending process, which can enhance the contact area between the electrode material and the solid electrolyte [59]. When the bending angle is 135°, the specific capacitance decreases because of the damaged electrode structure. Fig. 11B shows CV curves of folding and twisting. The specific capacitance becomes 111 % in the folding and 84 % in the twisting state. Fig. 11C shows the variation of specific capacitance of the flexible supercapacitor under different bending states. The comparison shows that the specific capacitance retains more than 84 % even after various bends. In conclusion, the device still has good performance under various deformations. Therefore, it is suitable for wearable devices. While dynamic fatigue cycling and long-term encapsulation tests were not included in this study, the stable performance under repeated static deformation provides strong evidence of structural resilience and flexible compatibility. These aspects will be the focus of future investigations to further validate practical deployment.

4. Conclusion

In this study, we developed a sustainable strategy for fabricating porous carbon materials from Setaria viridis stalks via controlled

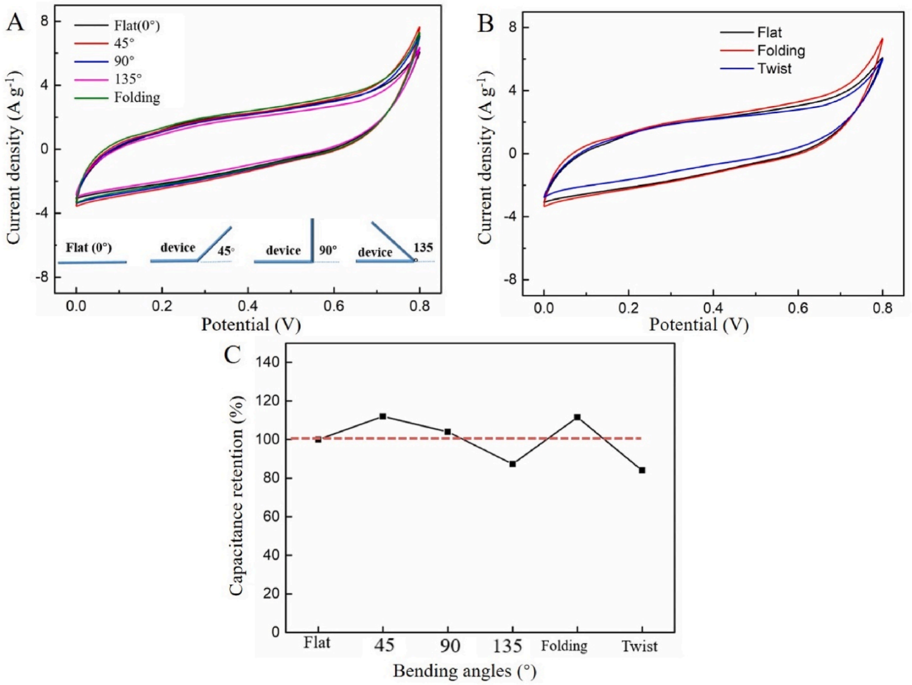

Fig. 11. Mechanical properties of the SVS-900 flexible supercapacitor. (A) CV curves at various bending angles, (B) CV tests in torsional and double back states, (C) Specific capacitances of flexible supercapacitor under different bending states.

carbonization and KOH activation. The resulting SVS-900 material features a hierarchically porous structure and favorable electrochemical properties when applied as an electrode in flexible solid-state supercapacitors. Benefiting from its interconnected vascular-inspired architecture and optimized activation conditions, the SVS-900-based device achieved a high specific capacitance of 690 F g^{-1}, excellent cycling stability (89 % retention over 10,000 cycles), and reliable mechanical performance under various static deformation states.

These results demonstrate that biomass-derived carbon from Setaria viridis is a promising, low-cost, and structurally adaptable candidate for flexible energy storage applications. While the current study validates its electrochemical and mechanical performance under laboratory conditions, further investigations into dynamic fatigue behavior, long-term leakage current stability, and encapsulation strategies are needed to evaluate its practical viability. Moreover, practical considerations remain for large-scale application. The KOH activation step requires significant thermal energy and generates alkaline effluents that must be neutralized or recycled. Additionally, long-term exposure of the biochar electrode to a humid environment may accelerate surface reactions and reduce cycle life. Recent studies highlight that advances in energy-efficient heating, closed-loop chemical recovery, and environmental encapsulation will be critical to improve cost-effectiveness and eco-friendliness of biomass-derived carbons.

CRediT authorship contribution statement

Wei Jin: Writing – original draft, Methodology, Investigation, Formal analysis, Data curation. **Wen Li:** Writing – original draft, Methodology, Investigation, Formal analysis, Data curation. **Rongke Sun:** Formal analysis. **Xiao Zhang:** Methodology. **Mingyu Wu:** Formal analysis. **Hafiza Sana Haider:** Writing – review & editing. **Dongliang Ma:** Investigation. **Yanqing Ma:** Writing – review & editing, Validation, Supervision, Project administration. **Lei Ma:** Writing – review & editing, Supervision, Methodology, Funding acquisition.

Statements and declarations

All data and code generated or used during the study appear in the submitted article.

Declaration of competing interest

The authors declare that they have no known competing financial interests or personal relationships that could have appeared to influence the work reported in this paper.

Acknowledgements

This work was financially supported by the National Key R & D Program of China (No. 2022YFC3006303).

Appendix A. Supplementary data

Supplementary data to this article can be found online at https://doi.org/10.1016/j.jics.2025.102074.

References

[1] J.M. Lee, G. Singh, W. Cha, S. Kim, J. Yi, S.-J. Hwang, A. Vinu, ACS Energy Lett. 5 (2020) 1939–1966.
[2] P.A. Shinde, L.K. Shrestha, K. Ariga, Green Energy Environ. (2025). http://doi.org/10.1016/j.gee.2025.02.007.
[3] Y. Yan, Y. Zhou, Y. Li, Y. Liu, Carbon Lett. 33 (2023) 1461–1483.
[4] B. Pal, J.B. Matsoso, A.K. Parameswaran, P.K. Roy, D. Lukas, J. Luxa, P. Marvan, J. Azadmanjiri, Z. Hrdlicka, R. Jose, Z. Sofer, Electrochim. Acta 415 (2022) 140239.
[5] Y. Gogotsi, P. Simon, Science 334 (2011) 917–918.
[6] S. Rajkumar, E. Elanthamilan, S.-F. Wang, H. Chryso, P.V.D. Balan, J.P. Merlin, Resour. Conserv. Recycl. 180 (2022) 106180.
[7] R. Srinivasan, E. Elaiyappillai, E.J. Nixon, I. Sharmila Lydia, P.M. Johnson, Inorg. Chim. Acta. 502 (2020) 119393.
[8] M. Barczak, T.J. Bandosz, Electrochim. Acta 305 (2019) 125–136.
[9] J. Serafin, M. Ouzzine, C. Xing, H. El Ouahabi, A. Kamińska, J. Sreńscek-Nazzal, J. CO2 Util. 62 (2022) 102071.
[10] D.P. Dubal, N.R. Chodankar, D.H. Kim, P. Gomez-Romero, Chem. Soc. Rev. 47 (2018) 2065–2129.
[11] G. Jiang, R.A. Senthil, Y. Sun, T.R. Kumar, J. Pan, J. Power Sources 520 (2022).
[12] C. Yuan, H. Xu, S.A. El-khodary, G. Ni, S. Esakkimuthu, S. Zhong, S. Wang, Fuel (2024) 362.
[13] L. Wei, G. Yushin, Nano Energy 1 (2012) 552–565.
[14] E. Frackowiak, F. Béguin, Carbon 39 (2001) 937–950.
[15] P. Simon, Y. Gogotsi, Nat. Mater. 7 (2008) 845–854.
[16] M. Sevilla, R. Mokaya, Energy Environ. Sci. 7 (2014) 1250–1280.
[17] A. Ilnicka, M. Skorupska, M. Szkoda, Z. Zarach, P. Kamedulski, W. Zielinski, J. P. Lukaszewicz, Sci. Rep. 11 (2021) 18387.
[18] J. Serafin, M. Baca, M. Biegun, E. Mijowska, R.J. Kaleńczuk, J. Sreńscek-Nazzal, B. Michalkiewicz, Appl. Surf. Sci. 497 (2019).
[19] J. Sreńscek-Nazzal, J. Serafin, A. Kamińska, A. Dymerska, E. Mijowska, B. Michalkiewicz, J. Colloid Interface Sci. 627 (2022) 978–991.
[20] D. Hulicova-Jurcakova, M. Seredych, G.Q. Lu, T.J. Bandosz, Adv. Funct. Mater. 19 (2009) 438–447.
[21] W. Du, Z. Zhang, L. Du, X. Fan, Z. Shen, X. Ren, Y. Zhao, C. Wei, S. Wei, J. Alloys Compd. 797 (2019) 1031–1040.
[22] J. Bao, H. Lu, D. Pei, C. Liang, Y. Chen, Nanotechnology 31 (2020).
[23] J. Chmiola, G. Yushin, Y. Gogotsi, C. Portet, P. Simon, P.L. Taberna, Science 313 (2006) 1760–1763.
[24] Z. Shang, X. An, H. Zhang, M. Shen, F. Baker, Y. Liu, L. Liu, J. Yang, H. Cao, Q. Xu, H. Liu, Y. Ni, Carbon 161 (2020) 62–70.
[25] Y. Li, L. Ni, J. Luo, L. Zhu, X. Zhang, H. Li, I. Zada, J. Yu, S. Zhu, K. Lian, Y. Li, D. Zhang, Adv. Funct. Mater. 34 (2024) 2403448.
[26] P. Han, M. Cheng, D. Luo, W. Cui, H. Liu, J. Du, M. Wang, Y. Zhao, L. Chen, C. Zhu, J. Xu, Energy Storage Mater. 24 (2020) 486–494.
[27] Q. Wang, Y. Qu, J. Bai, Z. Chen, Q. Luo, H. Li, J. Li, W. Yang, Nano Energy 120 (2024) 109147.
[28] G. Zhu, L. Ma, H. Lv, Y. Hu, T. Chen, R. Chen, J. Liang, X. Wang, Y. Wang, C. Yan, Z. Tie, Z. Jin, J. Liu, Nanoscale 9 (2017) 1237–1243.
[29] Y.S. Yun, S.Y. Cho, J. Shim, B.H. Kim, S.J. Chang, S.J. Baek, Y.S. Huh, Y. Tak, Y. W. Park, S. Park, H.J. Jin, Adv. Mater. 25 (2013) 1993–1998.
[30] X. Wei, B. Qiu, L. Xu, Q. Qin, W. Zhang, Z. Liu, F. Wei, Y. Lv, J. Energy Storage 62 (2023).
[31] O. Boujibar, A. Ghosh, O. Achak, T. Chafik, F. Ghamouss, J. Energy Storage 26 (2019) 100958.
[32] J. Li, K. Han, D. Wang, Z. Teng, Y. Cao, J. Qi, M. Li, M. Wang, Carbon 164 (2020) 42–50.
[33] Z. Pang, G. Li, X. Zou, C. Sun, C. Hu, W. Tang, L. Ji, H.-Y. Hsu, Q. Xu, X. Lu, J. Energy Chem. 56 (2021) 512–521.
[34] M.-C. Cheng, Y.-S. Chang, D.-C. Tsai, Y.-L. Huang, F.-S. Shieu, Fuel 387 (2025) 133790.
[35] M. Enterría, F.J. Martín-Jimeno, F. Suárez-García, J.I. Paredes, M.F.R. Pereira, J. I. Martins, A. Martínez-Alonso, J.M.D. Tascón, J.L. Figueiredo, Carbon 105 (2016) 474–483.
[36] M. Seredych, M. Koscinski, M. Sliwinska-Bartkowiak, T.J. Bandosz, ACS Sustain. Chem. Eng. 1 (2013) 1024–1032.
[37] M. Seredych, M. Koscinski, M. Sliwinska-Bartkowiak, T.J. Bandosz, J. Power Sources 220 (2012) 243–252.
[38] S. Zhang, N. Pan, Adv. Energy Mater. 5 (2014).
[39] Y. Xu, Z. Lin, X. Zhong, X. Huang, N.O. Weiss, Y. Huang, X. Duan, Nat. Commun. 5 (2014) 4554.
[40] C. Yang, S. Yun, J. Shi, M. Sun, N. Zafar, A. Arshad, Y. Zhang, L. Zhang, Chem. Eng. J. 419 (2021) 129636.
[41] A. Samage, M. Halakarni, H. Yoon, N. Sanna Kotrappanavar, Carbon 219 (2024) 118774.
[42] X. Wei, B. Qiu, L. Xu, Q. Qin, W. Zhang, Z. Liu, F. Wei, Y. Lv, J. Energy Storage 62 (2023) 106900.
[43] V. Augustyn, P. Simon, B. Dunn, Energy Environ. Sci. 7 (2014).
[44] S. Lu, W. Yang, M. Zhou, L. Qiu, B. Tao, Q. Zhao, X. Wang, L. Zhang, Q. Xie, Y. Ruan, J. Colloid Interface Sci. 610 (2022) 1088–1099.
[45] B. Peng, Y. Zhu, S. Chu, H. Zhang, Chem. Eng. J. 507 (2025) 160551.
[46] R. Yuksel, N. Karakehya, Carbon 221 (2024) 118934.
[47] A. Khan, R.A. Senthil, J. Pan, S. Osman, Y. Sun, X. Shu, Electrochim. Acta 335 (2020) 135588.
[48] M.-F. Wu, C.-H. Hsiao, C.-Y. Lee, N.-H. Tai, ACS Omega 5 (2020) 14417–14426.
[49] H. Liu, W. Shi, H. Song, Y. Chang, L. Feng, W. Hou, Y. Li, Y. Zhao, S. Zhu, G. Han, ACS Appl. Energy Mater. 6 (2022) 222–232.
[50] J. Pedro Aguiar dos Santos, F. Cesar Rufino, J.I. Yutaka Ota, R.C. Fernandes, R. Vicentini, C.J.B. Pagan, L. Morais Da Silva, H. Zanin, J. Energy Chem. 80 (2023) 265–283.
[51] K. Xia, Y. Cheng, H. Zhang, F. Han, L. Duan, X. Liu, J. Inorg. Organomet. Polym. Mater. 33 (2023) 2023–2034.
[52] X. Liu, S. Zhang, X. Wen, X. Chen, Y. Wen, X. Shi, E. Mijowska, Sci. Rep. 10 (2020) 3518.
[53] Q. Xu, X. Ni, S. Chen, J. Ye, J. Yang, H. Wang, D. Li, H. Yuan, Int. J. Hydrogen Energy 48 (2023) 25635–25644.

[54] M. Xie, H. Lin, G. Liu, H. Yang, H. Hu, H. Dong, Y. Liu, X. Liu, Y. Xiao, J. Energy Storage 96 (2024) 112670.

[55] H.-Y. Chung, G.-T. Pan, Z.-Y. Hong, C.-T. Hsu, S. Chong, T.C.-K. Yang, C.-M. Huang, Molecules 25 (2020) 4050.

[56] H. Li, T. Du, Q. Wang, J. Guo, S. Zhang, Y. Lu, J. Energy Storage 66 (2023) 107397.

[57] K. Chen, S. Weng, J. Lu, J. Gu, G. Chen, O. Hu, X. Jiang, L. Hou, Microporous Mesoporous Mater. 320 (2021) 111106.

[58] H. Yang, J. Zhou, M. Wang, S. Wu, W. Yang, H. Wang, Int. J. Energy Res. 44 (2020) 4449–4463.

[59] Q. Niu, Q. Tang, X. Sun, L. Wang, K. Gao, J. Mater. Sci. 57 (2022) 5154–5166.